remote sensing

MDPI

Article

Spatiotemporal Analysis of Atmospheric Chemical Potential Anomalies Associated with Major Seismic Events (Ms $\geq$ 7) in Western China: A Multi-Case Study

Qijun Jiao [1], Qinqin Liu [2,3,*], Changgui Lin [4], Feng Jing [5], Jiajun Li [2,3,6], Yuxiang Tian [2,3,6], Zhenxia Zhang [1] and Xuhui Shen [2,3]

[1] National Institute of Natural Hazards, Ministry of Emergency Management of China, Beijing 100085, China; jiaoqijun22@mails.ucas.ac.cn (Q.J.); zxzhang2018@163.com (Z.Z.)
[2] State Key Laboratory of Space Weather, National Space Science Center, Chinese Academy of Sciences, Beijing 100190, China; lijiajun22@mails.ucas.ac.cn (J.L.); tianyuxiang23@mails.ucas.ac.cn (Y.T.); shenxuhui@nssc.ac.cn (X.S.)
[3] Key Laboratory of Solar Activity and Space Weather, National Space Science Center, Chinese Academy of Sciences, Beijing 100190, China
[4] Key Laboratory of Microwave Remote Sensing Technology, National Space Science Center, Chinese Academy of Sciences, Beijing 100190, China; linchanggui@nssc.ac.cn
[5] Institute of Earthquake Forecasting, China Earthquake Administration, Beijing 100036, China; jingfeng@cea-ies.ac.cn
[6] School of Emergency Management Science and Engineering, University of Chinese Academy of Sciences, Beijing 100049, China
* Correspondence: liuqinqin@nssc.ac.cn; Tel.: +86-188-1318-1173

Abstract: Focusing on major earthquakes (EQs; MS $\geq$ 7) in Western China, this study primarily analyzes the fluctuation in Atmospheric Chemical Potential (ACP) before and after the Wenchuan, Yushu, Lushan, Jiuzhaigou, and Maduo EQs via Climatological Analysis of Seismic Precursors Identification (CAPRI). The distribution of vertical ACP revealed distinct altitude-dependent characteristics. The ACP at lower atmospheric layers (100–2000 m) exhibited a high correlation, and this correlation decreased with increasing altitude. Anomalies were detected within one month prior to each of the five EQs studied, with the majority occurring 14 to 30 days before the events, followed by a few additional anomalies. The spatial distribution of anomalies is consistent with the distribution of fault zones, with noticeable fluctuation in surrounding areas. The ACP at an altitude of 200 m gave a balance between sensitivity to seismic signals and minimal surface interference and proved to be optimal for EQ monitoring in Western China. The results offer a significant reference for remote sensing studies related to EQ monitoring and the Lithosphere–Atmosphere–Ionosphere Coupling (LAIC) model, thereby advancing our understanding of pre-seismic atmospheric variations in Western China.

Keywords: earthquake; seismic precursor; CAPRI algorithm; atmospheric chemical potential; temperature; relative humidity

check for updates

Academic Editors: Nicola Alessandro Pino, Stefano Carlino and Raffaele Castaldo

Received: 25 November 2024
Revised: 9 January 2025
Accepted: 13 January 2025
Published: 16 January 2025

Citation: Jiao, Q.; Liu, Q.; Lin, C.; Jing, F.; Li, J.; Tian, Y.; Zhang, Z.; Shen, X. Spatiotemporal Analysis of Atmospheric Chemical Potential Anomalies Associated with Major Seismic Events (Ms $\geq$ 7) in Western China: A Multi-Case Study. *Remote Sens.* **2025**, *17*, 311. https://doi.org/10.3390/rs17020311

Copyright: © 2025 by the authors. Licensee MDPI, Basel, Switzerland. This article is an open access article distributed under the terms and conditions of the Creative Commons Attribution (CC BY) license (https://creativecommons.org/licenses/by/4.0/).

1. Introduction

Earthquakes (EQs) are among the most severe and destructive geophysical disasters, posing significant threats to human life and infrastructure. For instance, the Wenchuan EQ on 12 May 2008 stands out as one of the most catastrophic continental EQ events in recent Chinese history. This disaster caused the deaths of more than ten thousand people across several cities in the Western Sichuan basin. Considering the lost productivity,

income, tax revenue, and costs associated with rebuilding infrastructure, the economic impact of a magnitude 7 or larger EQ is projected to exceed €100 billion. This situation will likely worsen due to the ongoing growth and concentration of human populations in urban centers, often located in seismic regions [1]. Early warning systems for EQs enable prompt evacuations and timely emergency responses. By implementing appropriate mitigation measures, damage to industry, transportation, and the power grid can be significantly reduced, thereby mitigating the overall impact. However, there remains a lack of monitoring tools that can accurately detect EQ precursors.

The preparation and occurrence of EQs involve highly complex geophysical processes, accompanied by material migration and energy release. Early efforts in EQ monitoring focused primarily on observing surface deformation and drilling underground. The development of ground stress monitoring methods was initially slow due to limitations in deep drilling technology and the accuracy of instrumentation [2]. Over time, seismic strain measurement gained popularity. Although this method offered high accuracy, the costs associated with manual drilling and instrumentation were significant, requiring considerable labor and resources, which limited its widespread use [3]. Research into the relationship between certain gases and seismic activity began in earnest in the late 1970s. However, predicting EQs based on these gases proved difficult because rock deformation, soil porosity, radionuclide composition, and weather conditions significantly influenced their concentrations and migration processes. As a result, the accuracy of EQ predictions based on gas measurements remained low [4]. In recent decades, researchers have been studying the electromagnetic phenomena associated with increased seismic activity. These phenomena occur from the early warning phases through to the actual EQ event. Monitoring electromagnetic signals during these precursory phases has the potential to provide short-term predictions of major EQs [5–10]. However, the vastness of seismic zones and the sparse, uneven distribution of fixed-point monitoring stations mean that many countries lack sufficient ground-based experimental facilities to monitor geophysical parameters effectively [11].

Currently, scientists use various remote sensing data with high timeliness and cost-effectiveness to monitor EQ precursors such as temperature [12,13], relative humidity [14], outgoing longwave radiation (OLR) [15–17], surface latent heat flux (SLHF) [18], gases [19], aerosol optical depth (AOD) [20,21], total electron content (TEC) in the ionosphere [22,23], magnetic and electric field intensity [24], crustal deformation [25], etc. According to He et al. [26], the Wenchuan EQ's multi-parametric precursors exhibited common phenomena before the event: widespread anomalies 3 months before, contraction near the fault zone 10 days prior, and the most prominent phenomena 2–7 days in advance. Anomalies in heat release, humidity, and other meteorological parameters can also be observed before and after EQs in the western region of China. Singh et al. [14] continuously monitored air temperatures before the Wenchuan EQ and found significant anomalies, suggesting a strong coupling between the lithosphere, atmosphere, and ionosphere associated with EQs. In the Sichuan–Qinghai region, scientists observed anomalies in brightness temperature 1–2 months before EQs, including short-term increases of 3–5 degrees Celsius before the events with elevated temperatures persisting for several hours to days afterward, which are attributed to the release of helium, radon, and carbon-containing gases from the subsurface [27–29]. Additionally, a strong correlation between water vapor and brightness temperature was found before the Wenchuan, Lushan, and Yushu EQs [12,30,31]. Moreover, the most significant anomalies in SLHF occurred 6 to 3 days before the Wenchuan and Yushu EQs, and it is suggested that changes in relative humidity near the epicenter before the Wenchuan EQ were similar to changes in air temperature and pressure [32,33].

According to Pulinets et al. [34], the Lithosphere–Atmosphere–Ionosphere Coupling (LAIC) model explains the EQ process as a synergy of processes occurring at the Earth's surface, in the atmosphere, and in the ionosphere. In seismically active fault zones, the release of radon gas ionizes the air, creating new ions that serve as nucleation centers for water vapor condensation, leading to the formation of large ion clusters. As the rate of ion production and concentration increase, the binding energy of water molecules to ions—and thus the chemical potential—also rises. However, due to ionization, the newly formed ions exhibit different chemical potentials. Therefore, within the one-component approximation, a correction to the chemical potential was introduced by Pulinets et al. [35], known as the Atmospheric Chemical Potential (ACP), which can be derived from temperature and relative humidity. Pulinets et al. [36] further proposed ACP to be a reliable short-term EQ precursor, as they found that the precursory variations in ACP exhibited a blow-up character, being outliers on the monthly time scale for several decades at given locations. ACP might be related to the release of radon in the atmosphere [37], thereby being potentially applied to detecting natural disasters such as EQs, volcanoes, and hurricanes [36].

However, research on ACP is currently limited and, to our best knowledge, has not yet been applied to EQ monitoring in China. In addition, ground station data have low spatial and temporal resolution, and satellite data are not suitable for ACP monitoring due to difficulty in obtaining the vertical characteristics of temperature and humidity parameters. In this study, we use reanalysis data named MERRA-2 [38], which include long-term data series and full spatial coverage, to analyze ACP in Western China. We first examined the variations in ACP at different altitudes and calculated the Pearson Correlation Coefficient (PCC). Subsequently, we employed the Climatological Analysis for Seismic Precursor Identification (CAPRI) algorithm [39] to reduce the effects of global warming and isolate the background field of ACP. Then, we compared it with the ACP values from the year of seismic activity to identify the dates of ACP anomalies. Finally, we analyzed the spatial distribution of these anomalies.

2. Materials and Methods

2.1. Study Area

The western region of China, located at the collision boundary between the Indian and Eurasian plates, is characterized by complex geological structures. This area is particularly prone to frequent seismic activity [40]. In the last two decades, five major EQs (Ms $\geq$ 7) have struck this region, causing widespread destruction and significant loss of life. The Wenchuan, Yushu, Lushan, Jiuzhaigou, and Maduo EQs were selected for analysis, and details are given in Table 1. The Longmenshan Fault (LMSF) zone, approximately 500 km long and 70 km wide, is located on the eastern margin of the Qinghai–Tibet Plateau and connects to the Sichuan Basin. It includes the Hill-Back Fracture, the Mid-Fracture, and the Hill-Front Fracture, along with their associated folds [41]. This fault zone was responsible for the Wenchuan and Lushan EQs. The Jiuzhaigou EQ occurred at the northern terminus of the Minshan Uplift Zone (MUZ), where several major faults intersect, including the Tazang Fault, the Northern Huya Fault, and the Minjiang Fault [42]. The Yushu EQ occurred on the Ganzi-Yushu Fault (GYF), part of the western segment of the Xianshuihe Fault system, a prominent left-lateral strike–slip fault in Eastern Tibet [43]. The Maduo EQ probably occurred on either the Kunlun Pass-Jiangcuo Fault (KPJF) or the Maduo-Gande Fault (MGF), both within the Bayan Har Block, about 70 km south of its northern boundary, the Eastern Kunlun Fault [44,45]. The spatial distribution of the selected study EQ cases is shown in Figure 1.

Table 1. Information on earthquakes (EQs) selected for this research.

Region	Time (UTC)	Lon (°E)	Lat (°N)	Ms	Depth (km)
Sichuan, Wenchuan	12 May 2008, 06:28	103.40	31.00	8.0	14
Qinghai, Yushu	13 April 2010, 23:49	96.60	33.10	7.1	33
Sichuan, Lushan	20 April 2013, 00:02	103.00	30.30	7.0	13
Sichuan, Jiuzhaigou	8 August 2017, 13:19	103.82	33.20	7.0	20
Qinghai, Maduo	21 May 2021, 18:04	98.34	34.59	7.4	17

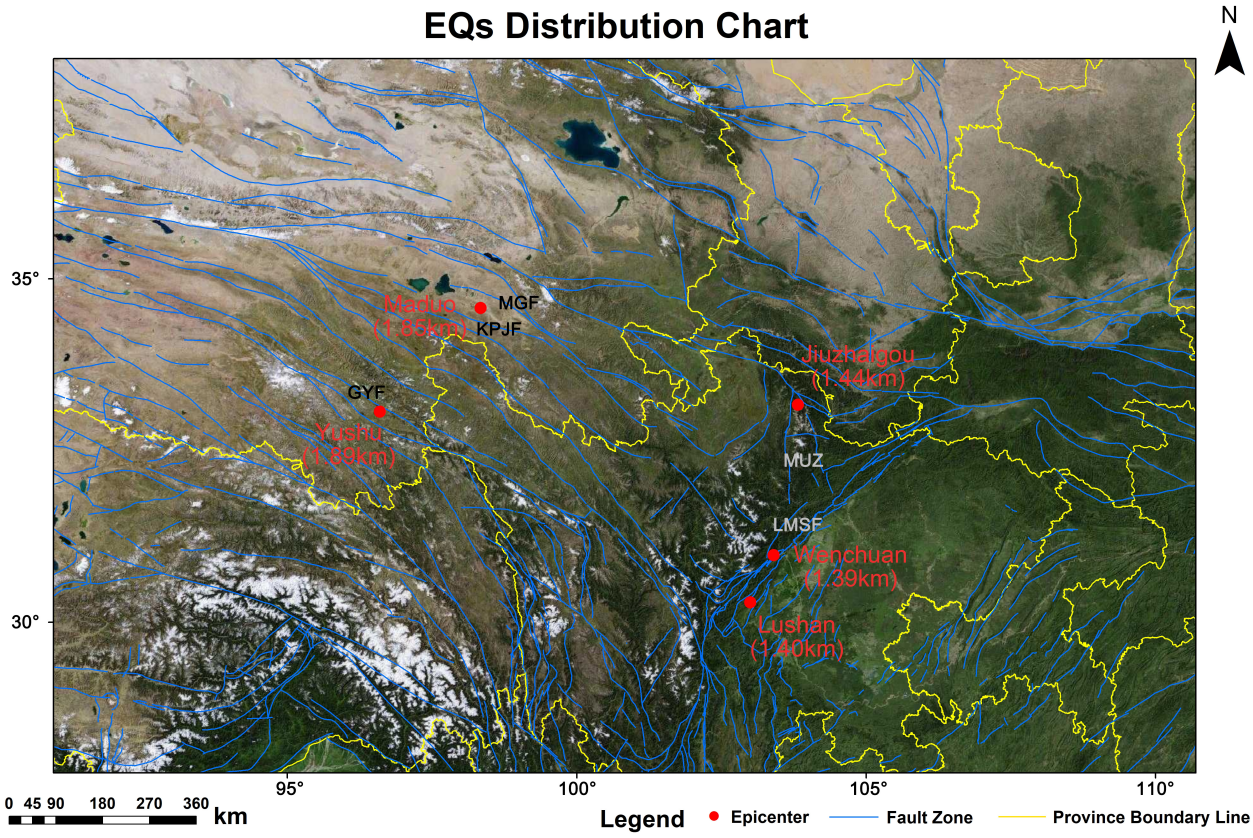

Figure 1. The epicenters, average altitudes, and associated fault zones of the five selected earthquakes (EQs) in this study. The average altitude data were derived by calculating the mean value within a 700 km half-side length centered on the epicenter, using the mid-layer height data from each model layer of MERRA-2. The red dots represent the epicenters, the blue solid lines represent the fault zones, and the yellow solid lines represent the provincial boundaries.

2.2. Data Collection

The dataset employed in this study is sourced from the Modern-Era Retrospective Analysis for Research and Applications-2 (MERRA-2), accessible via NASA's online database https://disc.gsfc.nasa.gov/datasets?project=MERRA-2 (accessed on 1 December 2024). This comprehensive dataset, a product of the Global Modeling and Assimilation Office (GMAO), is synthesized through the amalgamation of Goddard Earth Observing System (GEOS) climate simulations and meteorological observations from a diverse array of sources like the Moderate Resolution Imaging Spectroradiometer (MODIS), the Atmospheric InfraRed Sounder (AIRS), and the Ozone Monitoring Instrument (OMI), among various other sensors [38]. The timeframe spans from 2 April 1980 to the present, covering the entire globe with a spatial resolution of 0.5° × 0.625° (approximately 50 km). The data are in netCDF-4 format, with each set containing longitude, latitude, data dimensions, time dimensions, and a vertical dimension, which are divided into 72 layers based on

pressure. To reduce the impact of human activities on the data, the temperature and relative humidity data at 2:00 local time were uniformly selected for analysis. This study utilized the 3-hourly datasets of surface air temperature and atmospheric relative humidity from the inst3_3d_asm_nv dataset. To calculate the ACP at different altitudes, temperature and humidity data from the epicenter location were used, covering a period of 50 days, from 45 days before to 5 days after the EQ.

2.3. Methodology

2.3.1. Atmospheric Chemical Potential (ACP) Calculation

In the atmosphere, liquid water (water drops), water vapor, and ice crystals coexist, and the phase transitions between these states release or absorb latent heat. ACP is proposed to describe the latent heat fluxes created (or absorbed) during the abrupt phase transitions of water in the atmosphere. According to Pulinets et al. [35], the latent heat for water molecules at phase transitions is equal to its chemical potential, and it is equal to the work function when the molecule separates from the water droplet. In the one-component approximation, the relative humidity $H(t)$ can be expressed as follows:

$$H(t) = \frac{exp\left(\frac{-U(t)}{kT}\right)}{exp\left(\frac{-U_0}{kT}\right)} = exp\left(\frac{U_0 - U(t)}{kT}\right) = exp\left(-\frac{0.032\Delta U cos^2 t}{(kT)^2}\right), \quad (1)$$

where $U(t)$ is the work function in eV, t refers to time and is measured in radians, and $cos^2 t$ is used to take the daily changes of the solar radiation into account. In addition, k is the Boltzmann constant, T is the temperature in K, H is a unitless ratio, U_0 is the latent heat of evaporation, and ΔU is the required value of the chemical potential correction ACP. The conversion in the formula takes into account the state of energy at the boiling temperature ($kT = 8.625 \times 10^{-5} \times 373.15 = 0.032\ eV$) and ignores the difference between T and the boiling temperature.

Taking $cos^2 t = 1$ and inserting the value of the Boltzmann constant k in eV/K, Formula (1) can be presented as follows:

$$H = exp[-\frac{0.032\Delta U}{(8.625 \times 10^{-5} T)^2}], \quad (2)$$

Simplifying the above formula and converting the unit of H to % and T to °C:

$$ACP = \Delta U = 5.8 \times 10^{-10}(20T + 5463)^2 \ln(100/H), \quad (3)$$

where ACP is in eV.

2.3.2. Climatological Analysis for Seismic Precursor Identification (CAPRI)

To eliminate the effects of global warming and the warming and humidification in Western China, the CAPRI algorithm proposed by Piscini et al. [39] was employed. This method identifies anomalies in climate parameter time series through statistical analysis and removes anomalies from several years of same-season ACP data. Liu et al. [46] applied the CAPRI algorithm to monitor multi-parameter data for 90 days before the Wenchuan and Lushan EQs, demonstrating its suitability for EQ monitoring in Western China. Additionally, some researchers use the CAPRI algorithm in the analysis of Luding and Kahramanmaraş EQs [47,48]. When calculating the ACP time series using the CAPRI algorithm, the average data within a 700 km half-side length centered on the epicenter were used, covering a period of 3.5 months. The algorithm is illustrated below:

Before being processed, the data are spatially averaged using only those over the land:

$$A(d)_y = \langle A(d, \lambda, \psi)_y \rangle_{\lambda,\psi}, \tag{4}$$

where $A(d)_y$ is the mean value of ACP for the specific day d in the year y in the MERRA-2 data; λ, ψ are the latitude and longitude, respectively; and the triangular brackets represent the spatial average. This formula does not use post-EQ data; only data from 1980 to the year before the EQs.

Then, it removes the long-term trend over the whole day-by-day dataset. Using $m(d)$ as the fitting slope, the ACP values for the same day each year are linearly fitted, and the long-term variation in this variable is removed using the following equation:

$$A^{'}(d)_y = A(d)_y - m(d) \times (y - y_0). \tag{5}$$

Specifically, m represents the slope, and y_0 is the reference year, typically the first year of the dataset. After removing the long-term trend using the linear fitting slope $m(d)$, the average ACP value for each day over the past N_y years is calculated to obtain the seasonal mean ACP value:

$$A_h(d) = \frac{1}{N_y} \sum_{y_0}^{\tilde{y}-1} A^{'}(d)_y, \tag{6}$$

where N_y is the total number of years used to calculate the average, equal to $\tilde{y} - y_0$, and $\tilde{y}$ is the year in which EQs occurred. Additionally, the standard deviation for each day will be calculated and overlayed with historical data for comparison with the research data.

To make the data from the EQ year $\tilde{y}$ comparable with the processed historical data, the data from the EQ year are detrended so that their average value equals the average value of the historical data:

$$A(d)_{\tilde{y}} = A^{'}(d)_{\tilde{y}} - (\langle A^{'}_{\tilde{y}} \rangle_d - \langle A_h \rangle_d), \tag{7}$$

where triangular brackets stand for the calculation of the average over all dates d.

The above operations are used to distinguish short-term anomalies without considering the anomalies of a particular year relative to the average. Finally, we set the anomaly threshold as days where values exceeded the average by at least 2 standard deviations and proceeded with further analysis. To study the spatial variation of the ACP before and after the EQ, we first obtained the background field by removing the global warming effect using the CAPRI algorithm. Then, we identified the ACP data from the EQ year that was closest to the background field during the same period. Finally, we subtracted the distribution of the ACP on the day with the highest anomaly from the anomalous distribution of the EQ year to obtain the spatial distribution of the anomalies.

2.3.3. Statistical Analysis

This study uses Pearson's correlation coefficient to perform a correlation analysis of ACP curves at different altitudes, which is used to measure the degree of linear correlation between two sets of variables. PCC is defined as the ratio of the covariance of the two variables to the product of their standard deviations, with results ranging from -1 to 1. A value of 1 indicates a perfect positive correlation, 0 indicates no correlation, and -1 indicates a perfect negative correlation [49]. The formula for calculating PCC is as follows:

$$r = \frac{\sum_{i=1}^{n}(x_i - \overline{x})(y_i - \overline{y})}{\sqrt{\sum_{i=1}^{n}(x_i - \overline{x})^2}\sqrt{\sum_{i=1}^{n}(y_i - \overline{y})^2}}, \quad (8)$$

where r is PCC, and $\overline{x}$, $\overline{y}$ are the mean values of two variables.

3. Results

3.1. Vertical Distribution of ACP

The ACP at different altitudes is subject to various influences from surface conditions. To illustrate these differences at distinct altitudes, this study calculated and analyzed the ACP values of five EQs at eight altitude levels. For each EQ, the ACP value is derived through spatial averaging of all available grid points within a 700 km half-side length centered on the epicenter. Specifically, for each time point, we first identified all grid points within this range and then extract the temperature and relative humidity data for each identified grid point. Subsequently, we calculated the ACP value for each grid point. Finally, we computed the arithmetic mean of the ACP values of all grid points to obtain a single representative value for the entire area. The information on the selected levels and actual heights above the surface is comprehensively presented in Table 2. For the vertical distribution of ACP, we selected 45 days before and 5 days after the EQs as the EQ period.

Table 2. The selected temperature and relative humidity levels and the actual heights above the surface for different regions. The actual heights were derived by calculating the mean value within a 700 km half-length around the epicenter using the mid-layer height data from each model layer of the Modern-Era Retrospective Analysis for Research and Applications-2 (MERRA-2).

Level	Height (km)				
	Wenchuan	Yushu	Lushan	Jiuzhaigou	Maduo
72	0.07	0.05	0.07	0.09	0.07
71	0.20	0.17	0.20	0.22	0.19
68	0.57	0.53	0.57	0.59	0.55
64	1.09	1.03	1.09	1.11	1.05
58	2.12	2.01	2.12	2.13	2.04
50	5.08	4.83	5.08	5.06	4.85
43	10.32	9.85	10.32	10.26	9.87
33	20.30	19.82	20.28	20.26	19.87

As shown in Figure 2, the overall ACP fluctuates over time, and the legend shows the actual altitude. Each peak demonstrates a trend of decreasing ACP with increasing altitude. There is a peak each day around 14:00 local time. The ACP values at altitudes of 100 m to 1000 m show significant overlap, while the ACP at 2000 m exhibits slight variations compared to the lower altitudes. At altitudes of 5000 m and 10,000 m, the ACP shows a decreasing trend with increasing altitude during some peaks, but the amplitude of the fluctuations is much smaller than that of the lower altitudes. At 20,000 m, the ACP is almost unaffected by surface factors, and it shows stable variation. The ACPs exhibit a fluctuation range between 0.05 eV and 0.3 eV at lower altitudes, while at higher altitudes, the ACPs demonstrate a proximate fluctuation of around 0.4 eV.

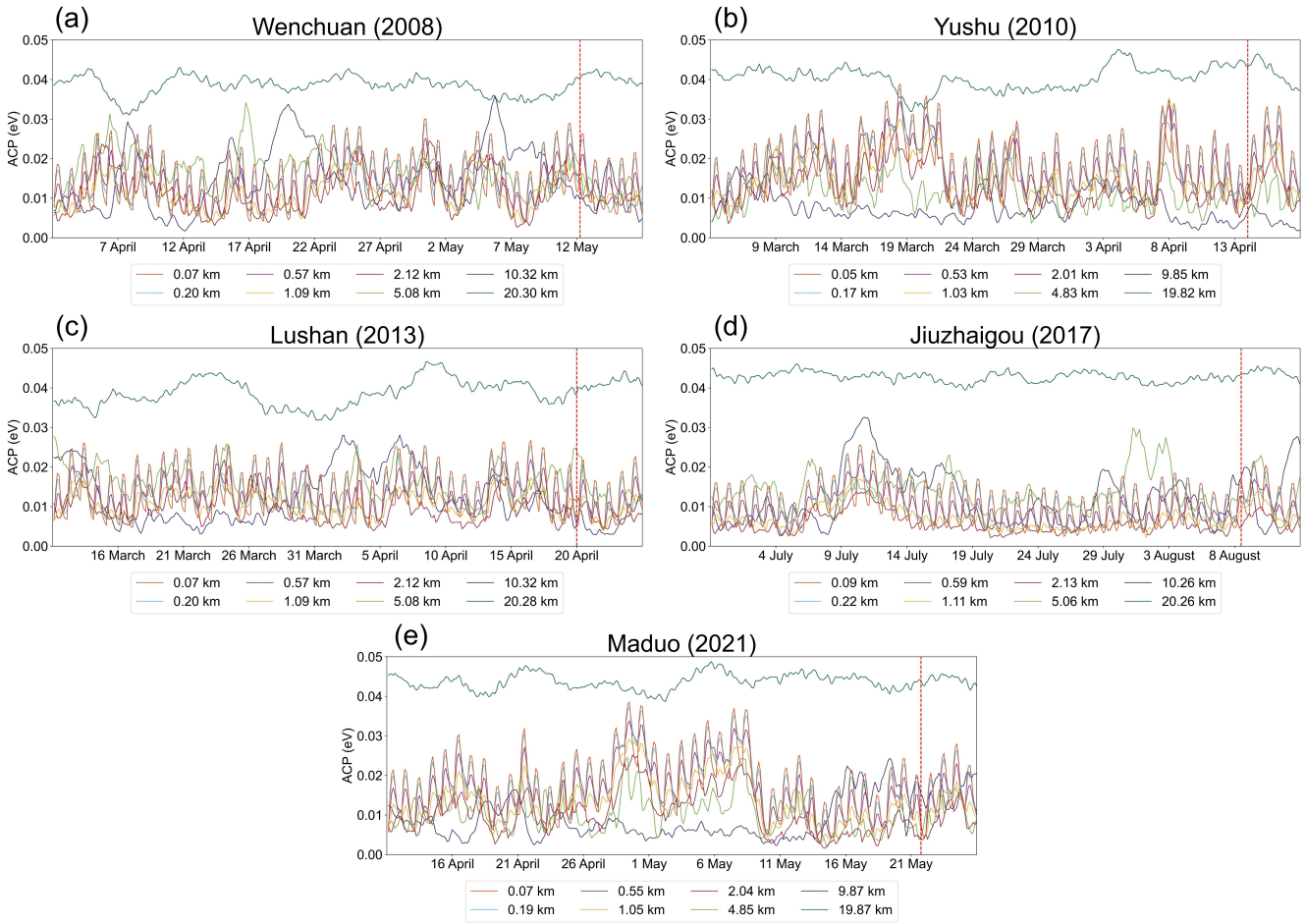

Figure 2. During the Wenchuan (**a**), Yushu (**b**), Lushan (**c**), Jiuzhaigou (**d**), and Maduo (**e**) EQs, Atmospheric Chemical Potential (ACP) variations were observed across eight distinct altitudinal strata during the EQ period, with data points recorded every 3 h. The ACP values in the figure represent the spatial average with the epicenter as the center and a half-side length of 700 km. The red dashed vertical line on the right represents the EQ occurrence.

In order to objectively compare the variations in the ACP at different altitudes, we calculated the PCC for each EQ from 45 days before to 5 days after the event at different altitudes. The results are presented in Figure 3. The findings indicate that the correlation between ACPs is negatively correlated with altitude. In particular, the correlation at 200 m is markedly higher, approximately 0.9, in comparison to both 100 m and 500 m. Conversely, at 1000 m, the correlation declines to approximately 0.8 in relation to 500 m and 2000 m, exhibiting minimal correlation with the lower ACP values. Moreover, altitudes of 5000 m, 10,000 m, and 20,000 m demonstrate negligible significance and almost no correlation with the lower ACP values. Therefore, we use the temperature and relative humidity data from level 71 (approximately 200 m) for subsequent analysis.

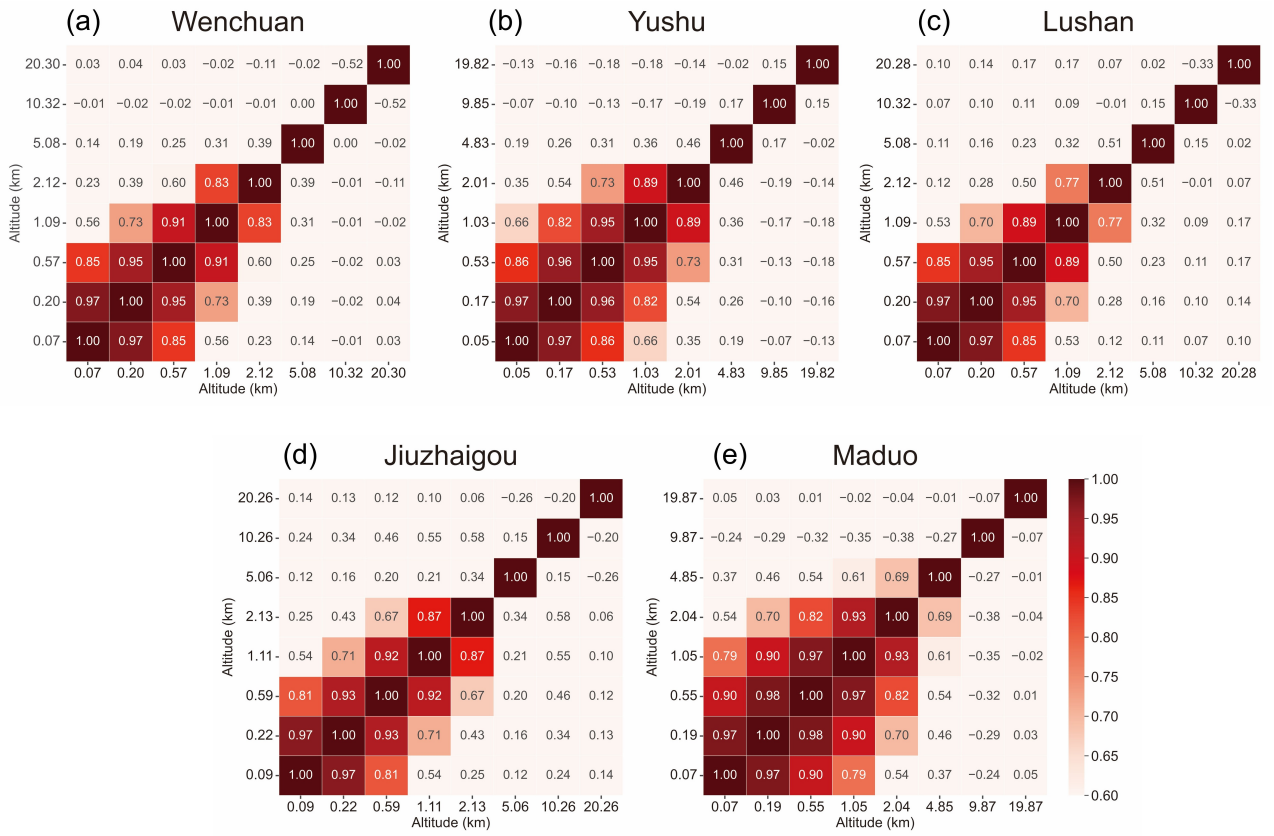

Figure 3. PCC (Pearson Correlation Coefficient) of ACPs at eight distinct altitudinal strata during the Wenchuan (**a**), Yushu (**b**), Lushan (**c**), Jiuzhaigou (**d**), and Maduo (**e**) EQ periods.

3.2. Temporal Evolution of ACP Anomalies

According to the previous research, we chose data at level 71 to analyze the anomalies of EQs. In this study, the ACP was within a 700 km half-side length of the epicenter, calculated before and after the EQs at 2:00 local time and compared with the background field to remove the global warming effect using the CAPRI algorithm. For the temporal evolution of ACP anomaly analysis, we selected 75 days before and 30 days after the EQs as the EQ period.

Figure 4 provides a statistical comparison of ACP values during specific years against historical data. Figure 4a presents a comparison between the ACP measurements from the Wenchuan EQ in 2008 and the background data collected from 1980 to 2007, specifically from 26 February to 12 June. The figure clearly illustrates that the ACP values on 28 February, 1 March, and 24 April exceeded the background value by more than 2σ. Similarly, Figure 4b sets the ACP values from the Yushu EQ in 2010 against the background data from 1980 to 2009, encompassing the period from 28 January to 13 May. The figure reveals that on 15 March, 18 March, 20 March, 7 April, 26 April, and 27 April, the ACP values exhibited anomalies. Figure 4c juxtaposes the ACP values from the Lushan EQ in 2013 with the background data spanning from 1980 to 2012, covering the period from 4 February to 20 May. It indicates that on 4 March, 7 March, and 12 March, the ACP values deviated significantly from the background. Figure 4d contrasts the ACP values from the Jiuzhaigou EQ in 2017 with the background data from 1980 to 2016, spanning the period from 24 May to 8 August. The figure underscores that on 25 May, 26 May, 9 July, 10 July, and 9 August, the ACP values surpassed the background value by more than 2σ. Finally, Figure 4e compares the ACP values from the Maduo EQ in 2021 with the background data from 1980

to 2020, which covers the period from 7 March to 21 June. The figure demonstrates that on 14 March, 21 March, 22 March, and 7 May, the ACP values showed notable anomalies.

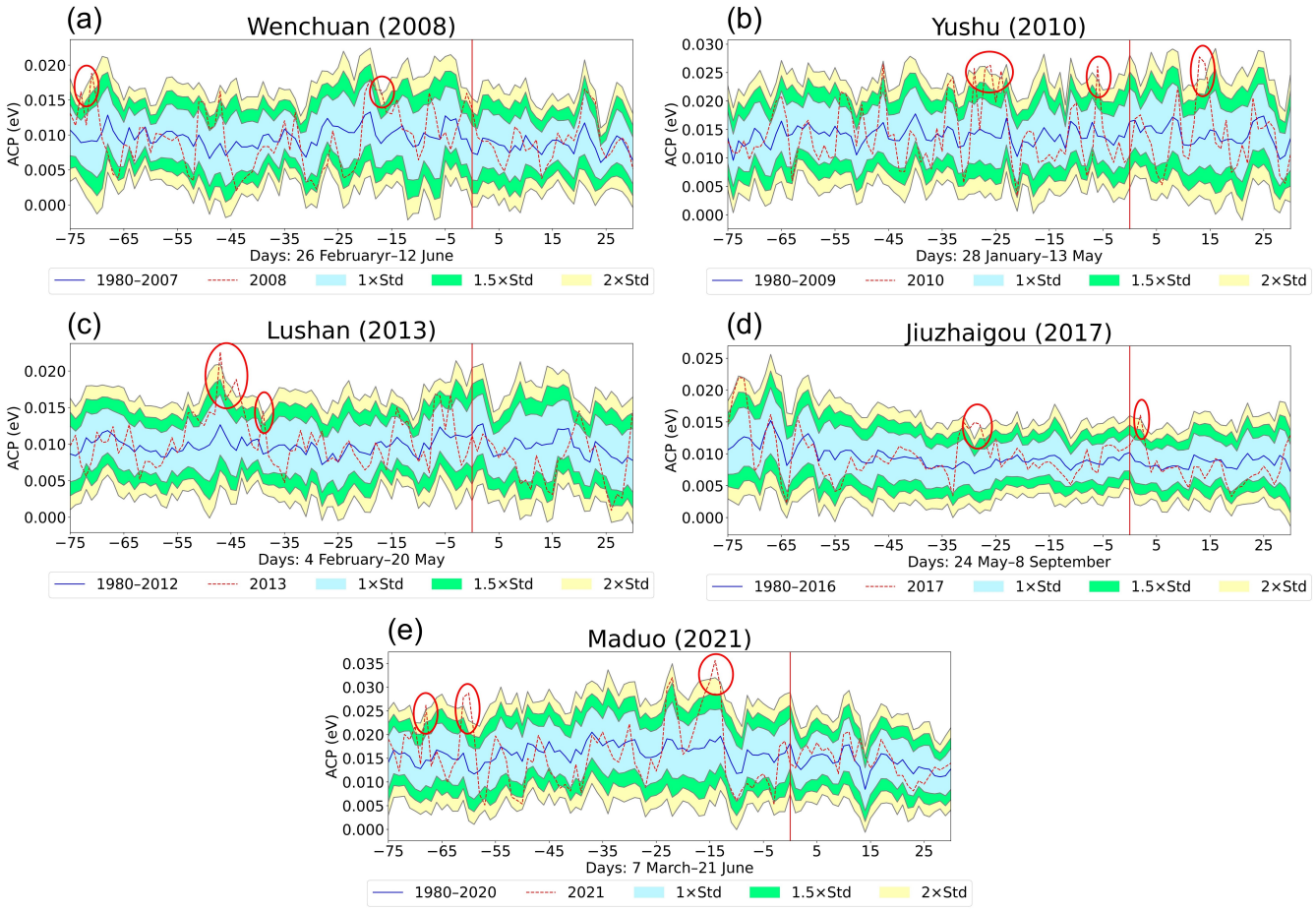

Figure 4. Monitoring maps of ACP anomalous (200 m) response at 18:00 during the EQ periods for Wenchuan (**a**), Yushu (**b**), Lushan (**c**), Jiuzhaigou (**d**), and Maduo (**e**) after removing the global warming effect using the CAPRI algorithm. Comparison of the time series (dashed red line) concerning the historical mean (continuous blue line). The stripes indicate 1.0 (cyan), 1.5 (green), and 2.0 (yellow) times the standard deviation. The red vertical line on the right represents EQ occurrence. The red circles indicate that anomalies greater than 2σ appeared.

Table 3 presents the dates on which anomalous ACP, exceeding 2σ, appeared for each EQ. For the Wenchuan EQ (a), anomalies were observed on days −74, −72, and −18. For the Yushu EQ (b), anomalies were noted on days −29, −26, −4, −6, 13, and 14. During the Lushan EQ (c), anomalies were apparent on days −47, −44, and −39. For the Jiuzhaigou EQ (d), anomalies were seen on days −29, −28, and 2. Lastly, during the Maduo EQ (e), anomalies were detected on days −68, −61, −60, and −14.

Table 3. The distribution showing the anomalous Atmospheric Chemical Potential (ACP) 75 days before the EQ and 30 days after the EQ. The red color highlights the anomalous days when their values exceeded 2σ.

Day	−75	−70	−65	−60	−55	−50	−45	−40	−35	−30	−25	−20	−15	−10	−5	0	5	10	15	20	25
Wenchuan	■	■										■									
Yushu										■	■	■			■			■			
Lushan						■	■	■													
Jiuzhaigou										■	■					■					
Maduo			■			■	■						■								

We selected the year 2020 as a control and plotted the anomaly time distribution for each EQ using the same spatial and temporal range as in Figure 4, with the results shown in Figure A1. The figures indicate that during periods without strong EQs, there were almost no anomalies in ACP.

3.3. Spatial Characteristics of ACP Anomalies

In order to investigate the spatial distribution of ACP anomalies before and after the seismic event, we first extracted the spatial distribution of ACP anomalies on dates exceeding 2σ. Subsequently, we identified the date for each EQ in Figure 4 during the year of EQ occurrence (indicated by the red dashed line) that most closely matched the mean of the historical data (represented by the blue solid line) as the reference date. Finally, we subtracted the spatial distribution of the reference date from that of the anomaly dates to obtain the anomalous spatial distribution.

During the Wenchuan EQ, the spatial distribution of ACP anomalies on specific days is illustrated in Figure 5. On 28 February, anomalies distributed along the fault zone emerged to the southwest and northeast of the epicenter. By 1 March, these anomalies had gradually intensified, with a high-value area also appearing to the southeast. By 24 April, the anomalies were concentrated in the northeast of the epicenter.

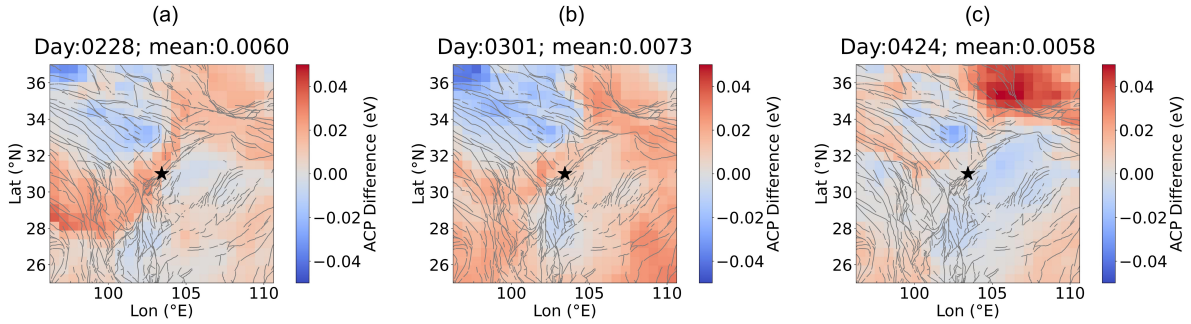

Figure 5. ACP anomaly distribution maps during the period of the 2008 Wenchuan EQ. These maps were obtained by subtracting the spatial distribution on the reference date (5 May) from the distributions on the anomaly dates 28 February (**a**), 1 March (**b**), and 24 April (**c**). "Mean" represents the spatial average of the figure. The epicenter is indicated by an asterisk in the figure, and grey lines indicate major faults in the study area.

For the Yushu EQ, the spatial distribution of ACP anomalies on specific days is depicted in Figure 6. On 15 March, a high ACP value area emerged around the epicenter, while a persistent low was observed in the southwest. By 18 March, this high-value area had intensified and expanded, then contracted toward the north and southeast of the epicenter. On 20 March, the anomalies in the north gradually weakened, while strong anomalies persisted in the southeast. On 7 April, the anomalies in the north intensified again, and strong anomalies reappeared in the south. By 26 April, the anomalies in both the north and south had gradually weakened, but on 27 April, strong anomalies reemerged in the northwest. Additionally, the anomalously high-value area developed along the fault zone, exhibiting significant fluctuations to the northwest and southeast of the epicenter.

The spatial distribution of ACP anomalies during the Lushan EQ is illustrated in Figure 7. On 4 March, a high ACP value area emerged to the north and west of the epicenter, while a persistent low was observed in the south. By 7 March, the anomalies had weakened to the west of the epicenter but intensified in the north. The northern anomalies disappeared by 12 March, reappearing in the northwest.

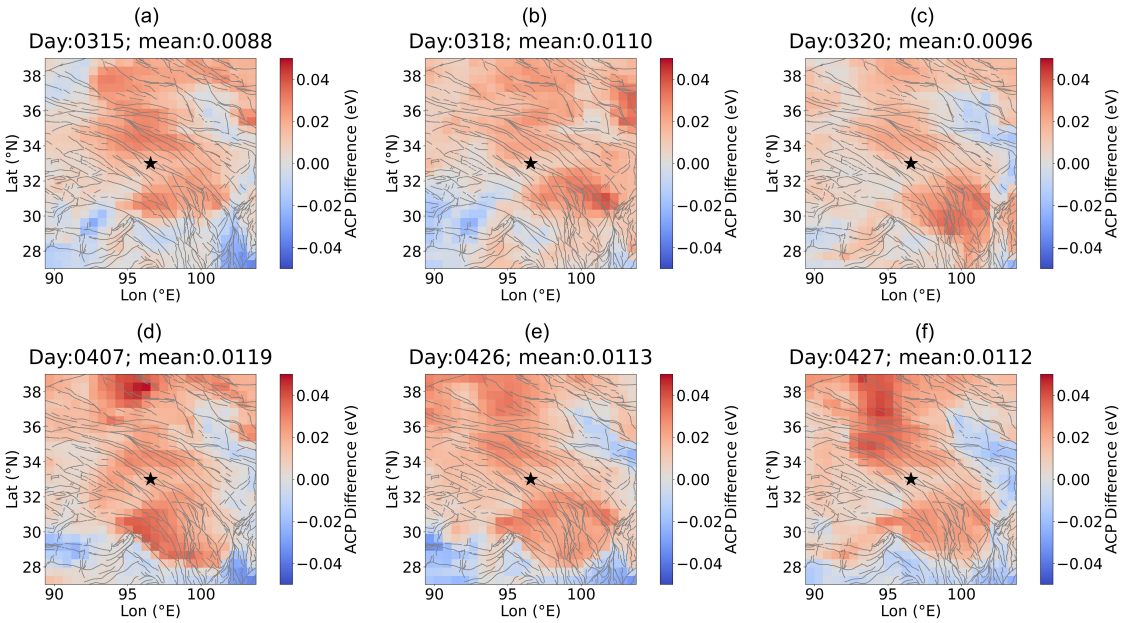

Figure 6. ACP anomaly distribution maps during the period of the 2010 Yushu EQ. These maps were obtained by subtracting the spatial distribution on the reference date (8 April) from the distributions on the anomaly dates 15 March (**a**), 18 March (**b**), 20 March (**c**), 7 April (**d**), 26 April (**e**), and 27 April (**f**). Labeled as shown in Figure 5.

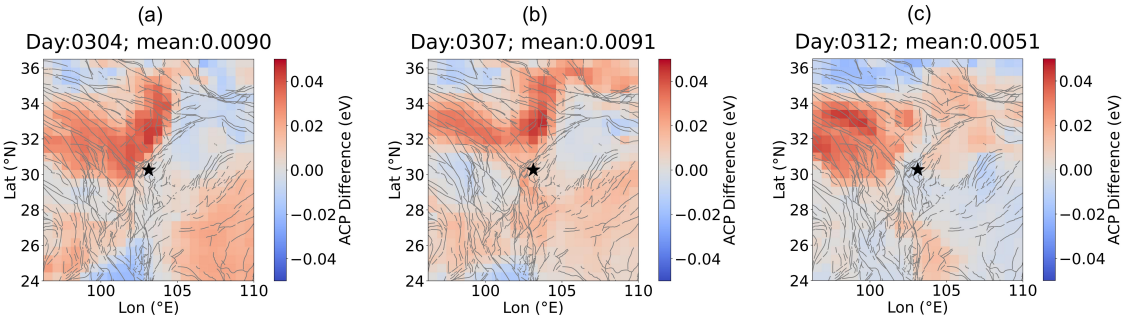

Figure 7. ACP anomaly distribution maps during the period of the 2013 Lushan EQ. These maps were obtained by subtracting the spatial distribution on the reference date (26 March) from the distributions on the anomaly dates 4 March (**a**), 7 March (**b**), and 12 March (**c**). Labeled as shown in Figure 5.

For the Jiuzhaigou EQ, the spatial distribution of ACP anomalies on specific days is depicted in Figure 8. On 9 July, anomalies appeared to the south and northeast of the epicenter, distributed along the fault zone. On 10 July, the area of anomalies in the north increased. By 9 August, the range of anomalies in the northeast and south had decreased, while anomalies in the west had intensified.

Lastly, the spatial distribution of ACP anomalies for the Maduo EQ on specific days is illustrated in Figure 9. On 14 March, anomalies appeared around the epicenter, with a concentration in the northeast. By 21 March, the anomalies in the northeast had weakened, while those in the southwest had intensified. On 22 March, anomalies around the epicenter and to the north intensified again, gradually decreasing by 7 May.

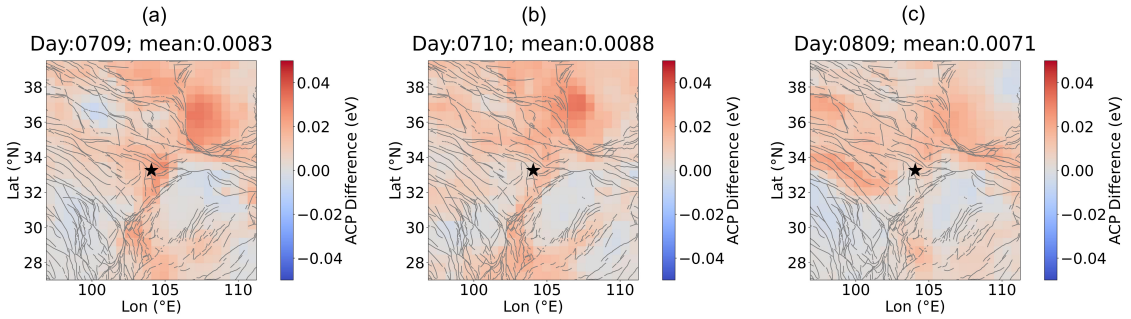

Figure 8. ACP anomaly distribution maps during the period of the 2017 Jiuzhaigou EQ. These maps were obtained by subtracting the spatial distribution on the reference date (14 August) from the distributions on the anomaly dates of 9 July (**a**), 10 July (**b**), and 9 August (**c**). Labeled as shown in Figure 5.

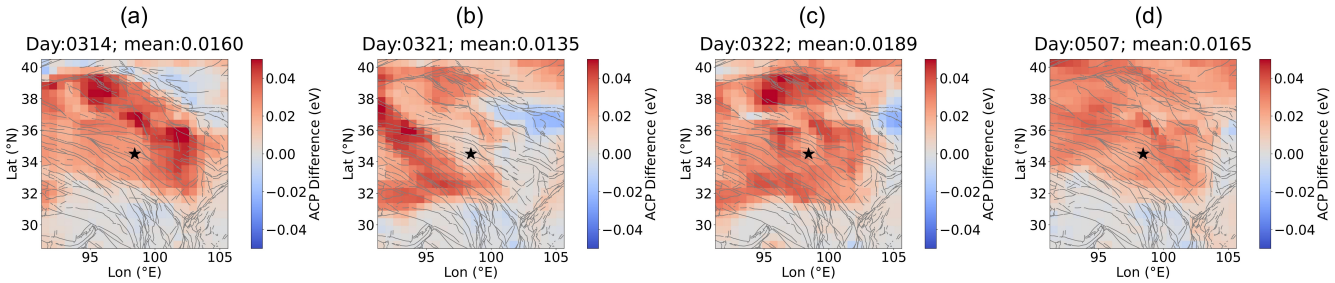

Figure 9. ACP anomaly distribution maps during the period of the 2017 Maduo EQ. These maps were obtained by subtracting the spatial distribution on the reference date (25 May) from the distributions on the anomaly dates of 14 March (**a**), 21 March (**b**), 22 March (**c**), and 7 May (**d**). Labeled as shown in Figure 5.

As a control, we selected different reference days for the five EQs and performed the same anomaly analysis, with the results shown in Figures A2–A6. The figures indicate that different reference days affect the intensity of the EQ anomalies but do not influence the overall distribution of the anomalies.

4. Discussion

This study analyzed ACP variations associated with five major EQs in Western China, revealing several significant patterns in vertical, temporal, and spatial distributions. The high-frequency (3-hourly) observations enabled detailed characterization of ACP dynamics at different altitudes. The temporal analysis demonstrated that ACP exhibits distinct diurnal variations, with peaks occurring at local noon and troughs at night, reflecting the strong influence of surface temperature patterns [13]. Notably, significant pre-seismic ACP anomalies were observed before each EQ, although their magnitudes and temporal evolution varied among different events.

Analysis of vertical ACP distributions revealed distinct altitude-dependent characteristics. According to Figure 2, the lower atmospheric layers (100–1000 m) exhibited highly correlated variations, suggesting a coherent response to seismic preparation processes. Particularly, measurements at 200 m altitude demonstrated optimal characteristics for EQ monitoring, as they maintained sufficient sensitivity to seismic-related signals while minimizing surface anthropogenic interference. This finding has important implications for establishing optimal monitoring protocols. In contrast, observations at higher altitudes (>2000 m) showed increasingly independent behavior, likely due to diminishing influence from surface processes and the growing impact of upper atmospheric dynamics.

The implementation of the CAPRI algorithm effectively isolated seismic-related ACP signals by removing long-term climate trends. Regional analysis revealed distinct background ACP characteristics: the Wenchuan, Lushan, and Jiuzhaigou regions showed similar background values (0.0088–0.0097 eV), while the Yushu and Maduo regions exhibited higher levels (0.0140–0.0151 eV). These systematic differences likely reflect the influence of regional topography and geological structures on atmospheric parameters. This spatial variability emphasizes the importance of considering local geological contexts when interpreting.

According to Table 3, anomalies were detected 14 to 30 days prior to the Wenchuan, Yushu, Jiuzhaigou, and Maduo EQs. Additionally, minor anomalies were observed 60 to 75 days before the Wenchuan and Maduo events. In Yushu and Jiuzhaigou, after an initial weakening, anomalies re-emerged 5 days before and persisted until 2 days after the EQs, with some continuing post-event. In the case of Lushan, anomalies appeared 39 to 49 days before the EQ and lasted for 15 days afterward. In summary, most anomalies were first detected 14 to 30 days before the EQs, with some anomalies occurring from 5 days before to 15 days after the events.

For the Wenchuan EQ, brightness temperature anomalies were observed on 25 April [13,50], consistent with the findings of our studies. Liu et al. reported that water vapor began accumulating on 5 April and peaked on 1 May, with the content dropping to its lowest level within the 40 days before and 10 days after the EQ [50]. These findings closely align with the results of this study. Similarly, for the Yushu EQ, lenticular clouds and OLR anomalies were observed on 14–15 March [51]. Additionally, Zheng et al. identified SLHF anomalies on 8–9 April [32], along with surface temperature anomalies on 10 April, which gradually dissipated starting from 26 April. Regarding the Lushan EQ, OLR anomalies were detected on 15 March [17]. Li et al. also noted that anomalies for the Wenchuan and Lushan EQs were concentrated 20–30 days before the events [37]. Moreover, for the Jiuzhaigou EQ, anomalies were found on 8 July in both temperatures of brightness blackbody and medium-wave infrared brightness [52].

By analyzing the spatial distribution of ACP anomalies, we found that the pre-EQ anomalies were mainly distributed around the epicenter, while the variations at the epicenter were relatively small. A comprehensive comparison reveals that the anomalies of the five EQs were distributed along the fault zones, with few occurrences in regions with no fault zone distribution. The ACP changes in areas without fault zones were relatively small and remained mostly stable. The anomaly distribution near the epicenter generally follows a trend of initial appearance, then re-strengthening, and subsequently weakening.

For the Wenchuan EQ, temperature anomalies were observed southwest of the epicenter [16], and microwave radiation anomalies occurred in the same region prior to the EQ [53]. Qin et al. [31] identified a micro-temperature anomaly near the epicenter before the Yushu EQ, which closely aligns with the spatial distribution of the anomalies observed in this study. Furthermore, for the Lushan EQ, researchers noted that the anomalies were primarily distributed northwest of the epicenter [35,54]. Additionally, thermal infrared anomalies were detected northwest and northeast of the epicenter during the Maduo EQ [24]. However, remote sensing studies on the Jiuzhaigou and Maduo EQs are fewer than those on the other three events. The observed patterns indicate that anomalies typically appear gradually three months before the EQs, then increase and intensify, showing a strong correlation with the fault zones and often manifesting in strip-like patterns. These findings are consistent with the results of this study.

5. Conclusions

In this study, we used reanalysis data to investigate the vertical distribution characteristics, temporal evolution patterns, and spatial features of ACPs in Western China. Our findings are as follows:

1. The ACPs at altitudes between 100 m and 1000 m show significant similarities, whereas at 2000 m they show slight fluctuations compared to other altitudes. Below 5000 m, the ACPs show a decreasing trend with altitude, while between 5000 and 10,000 m, they exhibit greater variability than at lower altitudes. Notably, at 20,000 m, the ACP remains almost unaffected by surface factors and stays in a stable variate state. To minimize the impact of anthropogenic activities on ACP, data at an altitude of 200 m are recommended for analyzing the Sichuan–Qinghai region;
2. In the five studied EQs, a consistent temporal pattern was observed: for each EQ, anomalies appeared two months prior, primarily concentrated 14 to 30 days before the event, with a few anomalies occurring afterward;
3. Spatially, the anomalies exhibited weaker variations in the epicentral region and more persistent changes in the surrounding areas, aligning closely with fault zone distributions.

This research highlights the applicability of ACP measurements at specific altitudes for the detection of seismic anomalies. The results provide a valuable reference for remote sensing studies related to EQ monitoring and the LAIC model, enhancing our understanding of pre-seismic atmospheric variations in Western China. However, as reanalysis data are derived from models rather than direct observations, the results inherently carry a degree of uncertainty. In addition, the relatively low spatial resolution of the data makes it difficult to analyze small-scale seismic phenomena accurately. Furthermore, large-scale weather events such as typhoons and cyclones can affect ACP results, reducing the accuracy of the monitoring results. In practical applications, ACP can be combined with multi-parameter observations to monitor and provide early warning of pre-seismic anomalies. Future research should incorporate higher-resolution remote sensing data for more rigorous analysis and delve deeper into the mechanisms of ACP generation and evolution.

Author Contributions: Conceptualization, Q.J., Q.L., C.L. and X.S.; methodology, Q.L. and C.L.; validation, Q.J. and Z.Z.; formal analysis, Q.J.; investigation, Q.J., J.L. and Y.T.; data curation, Q.J., J.L. and Y.T.; writing—original draft, Q.J.; writing—review and editing, Q.J., Q.L., C.L. and F.J.; supervision, X.S.; project administration, Q.L. and X.S. All authors have read and agreed to the published version of the manuscript.

Funding: This research was funded by the National Natural Science Foundation of China (Grant No. 42203082), Project No. E3RC2TQ5, and Project No. E3RC2TQ4.

Data Availability Statement: The MERRA-2 data are publicly available at https://disc.gsfc.nasa.gov/datasets?project=MERRA-2, accessed on 1 December 2024.

Acknowledgments: We would like to express our sincere gratitude to the National Space Science Centre (NSSC) of the Chinese Academy of Sciences for the financial support provided for this work. We also acknowledge NASA for providing us with data for the given work.

Conflicts of Interest: The authors declare no conflicts of interest.

Appendix A

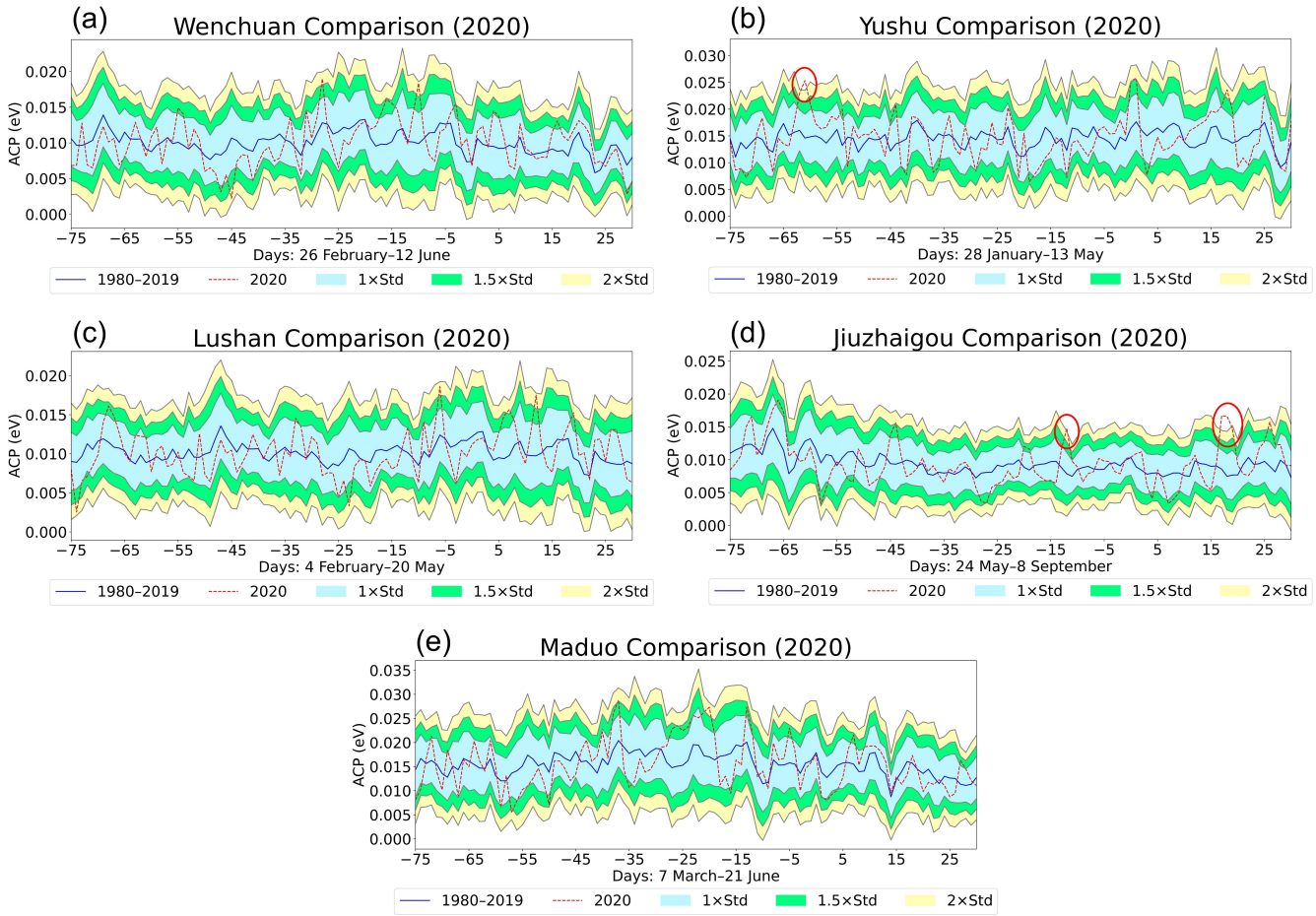

Figure A1. Monitoring maps of ACP anomalous (200 m) response at 18:00 in 2020 during the EQ periods for Wenchuan (**a**), Yushu (**b**), Lushan (**c**), Jiuzhaigou (**d**), and Maduo (**e**) after removing the global warming effect using the CAPRI algorithm. Labeled as shown in Figure 4.

Appendix B

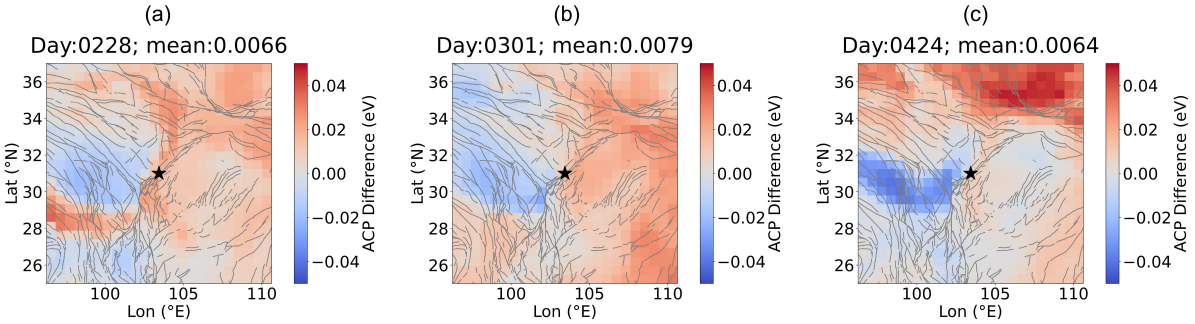

Figure A2. ACP anomaly distribution maps during the period of the 2008 Wenchuan EQ. These maps were obtained by subtracting the spatial distribution on the reference date (7 March) from the distributions on the anomaly dates of 28 February (**a**), 1 March (**b**), and 24 April (**c**). "Mean" represents the spatial average of the figure. Labeled as shown in Figure 5.

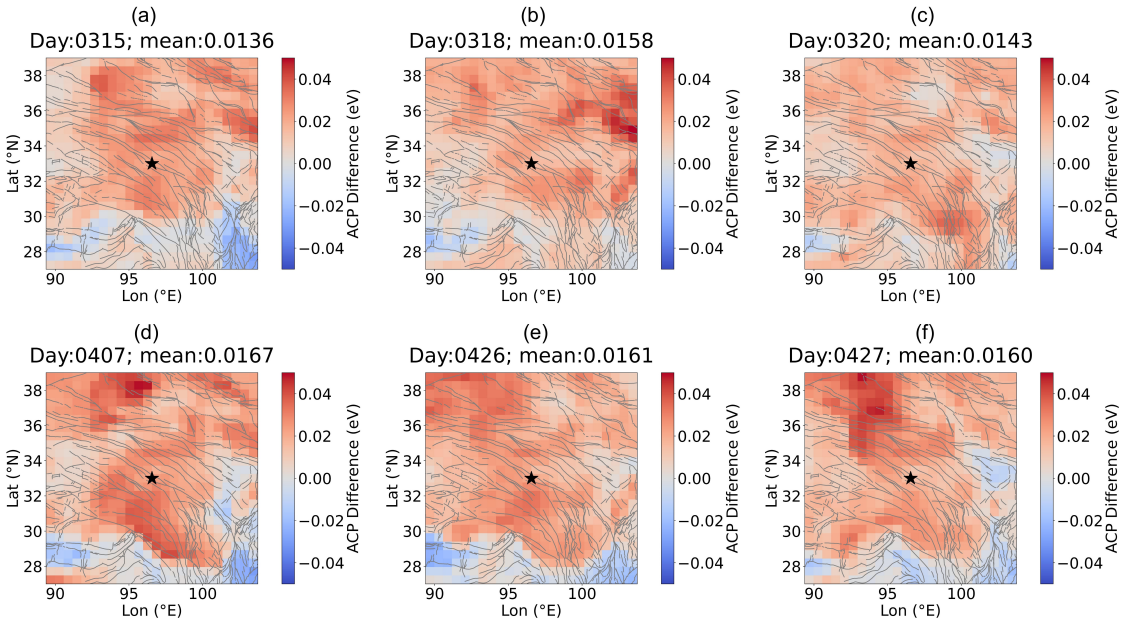

Figure A3. ACP anomaly distribution maps during the period of the 2010 Yushu EQ. These maps were obtained by subtracting the spatial distribution on the reference date (27 February) from the distributions on the anomaly dates of 15 March (**a**), 18 March (**b**), 20 March (**c**), 7 April (**d**), 26 April (**e**), and 27 April (**f**). Labeled as shown in Figure 5.

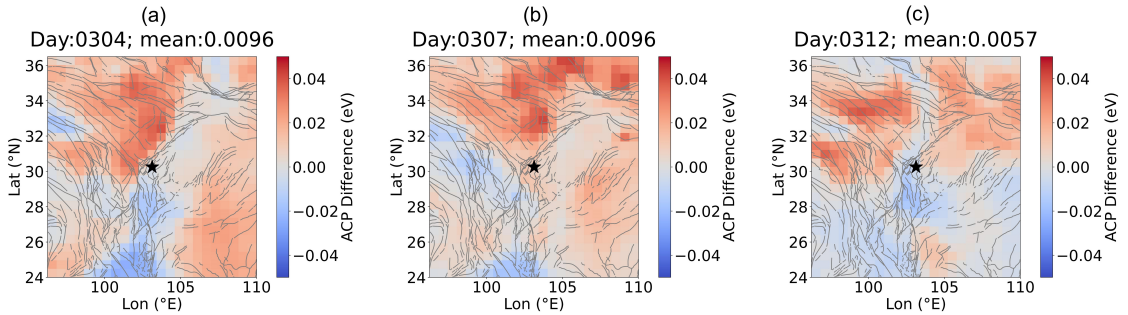

Figure A4. ACP anomaly distribution maps during the period of the 2013 Lushan EQ. These maps were obtained by subtracting the spatial distribution on the reference date (20 March) from the distributions on the anomaly dates of 4 March (**a**), 7 March (**b**), and 12 March (**c**). Labeled as shown in Figure 5.

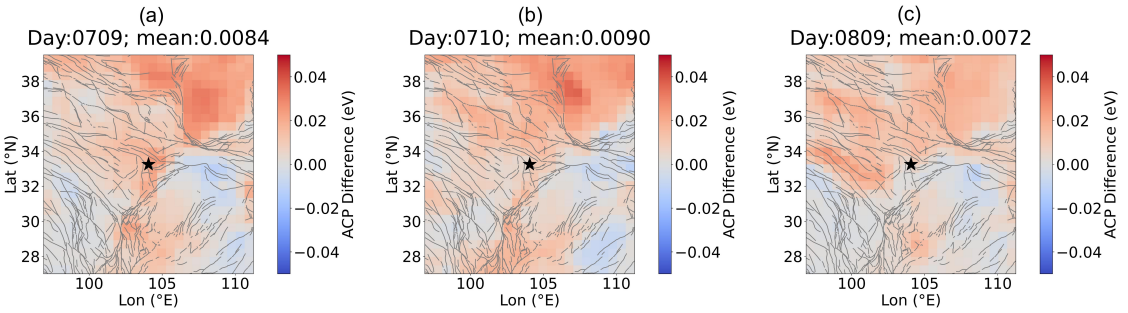

Figure A5. ACP anomaly distribution maps during the period of the 2017 Jiuzhaigou EQ. These maps were obtained by subtracting the spatial distribution on the reference date (3 July) from the distributions on the anomaly dates of 9 July (**a**), 10 July (**b**), and 9 August (**c**). Labeled as shown in Figure 5.

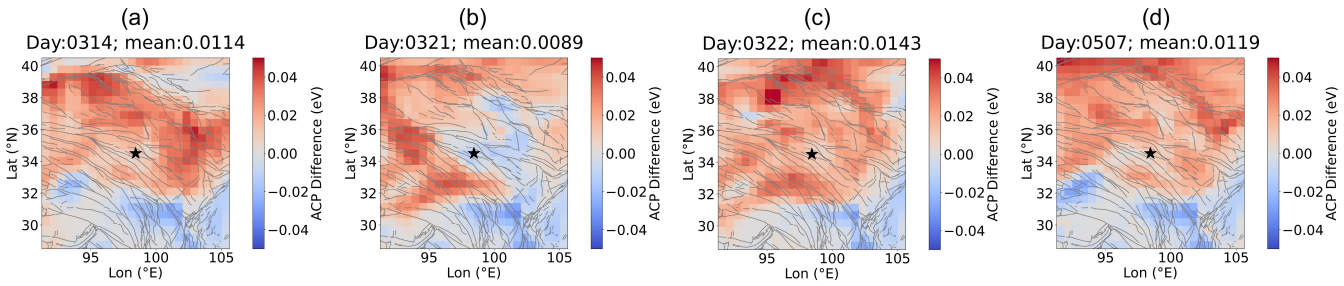

Figure A6. ACP anomaly distribution maps during the period of the 2017 Maduo EQ. These maps were obtained by subtracting the spatial distribution on the reference date (28 March) from the distributions on the anomaly dates of 14 March (**a**), 21 March (**b**), 22 March (**c**), and 7 May (**d**). Labeled as shown in Figure 5.

References

1. Freund, F.; Ouillon, G.; Scoville, J.; Sornette, D. Earthquake precursors in the light of peroxy defects theory: Critical review of systematic observations. *Eur. Phys. J. Spec. Top.* **2021**, *230*, 7–46. [CrossRef]
2. Zhao, X.; Pan, S.; Sun, Z.; Guo, H.; Zhang, L.; Feng, K. Advances of satellite remote sensing technology in earthquake prediction. *Nat. Hazards Rev.* **2021**, *22*, 03120001. [CrossRef]
3. Chen, Y. Earthquake prediction: Retrospect and prospect. *Sci. China Earth Sci.* **2009**, *3912*, 1633–1658.
4. Paudel, S.R.; Banjara, S.P.; Wagle, A.; Freund, F.T. Earthquake chemical precursors in groundwater: A review. *J. Seismol.* **2018**, *22*, 1293–1314. [CrossRef]
5. Varotsos, P.; Lazaridou, M. Latest aspects of earthquake prediction in Greece based on seismic electric signals. *Tectonophysics* **1991**, *188*, 321–347. [CrossRef]
6. Uyeda, S.; Kamogawa, M. The prediction of two large earthquakes in Greece. *Eos Trans. AGU* **2008**,*89*, 363. [CrossRef]
7. Orihara, Y.; Kamogawa, M.; Nagao, T.; Uyeda, S. Preseismic anomalous telluric current signals observed in Kozu-shima Island, Japan. *Proc. Natl. Acad. Sci. USA* **2012**, *109*, 19125–19128. [CrossRef]
8. Varotsos, P.A.; Sarlis, N.V.; Skordas, E.S. Identifying the occurrence time of an impending major earthquake: A review. *Earthq. Sci.* **2017**, *30*, 209–218. [CrossRef]
9. Sarlis, N.V.; Varotsos, P.A.; Skordas, E.S.; Uyeda, S.; Zlotnicki, J.; Nagao, T.; Rybin, A.; Lazaridou-Varotsos, M.S.; Papadopoulou, K.A. Seismic electric signals in seismic prone areas. *Earthq. Sci.* **2018**, *31*, 44–51. [CrossRef]
10. Uyeda, S.; Nagao, T.; Kamogawa, M. Short-term earthquake prediction: Current status of seismo-electromagnetics. *Tectonophysics* **2009**, *470*, 205–213. [CrossRef]
11. Shahrisvand, M.; Akhoondzadeh, M.; Sharifi, M.A. Detection of gravity changes before powerful earthquakes in GRACE satellite observations. *Ann. Geophys.* **2014**, *57*, A0543. [CrossRef]
12. Chen, H.; Jin, Y. Monitor the microwave thermal emission anomaly around the Yushu earthquake fault zone by using AMSR-E data. In Proceedings of the Remote Sensing of the Environment: The 17th China Conference on Remote Sensing, Hangzhou, China, 27–31 August 2010; SPIE: Bellingham, WA, USA, 2011; Volume 8203, pp. 184–190.
13. Zhang, Y.; Guo, X.; Zhong, M.; Shen, W.; Li, W.; He, B. Wenchuan earthquake: Brightness temperature changes from satellite infrared information. *Chin. Sci. Bull.* **2010**, *55*, 1917–1924. [CrossRef]
14. Singh, R.P.; Mehdi, W.; Gautam, R.; Senthil Kumar, J.; Zlotnicki, J.; Kafatos, M. Precursory signals using satellite and ground data associated with the Wenchuan Earthquake of 12 May 2008. *Int. J. Remote Sens.* **2010**, *31*, 3341–3354. [CrossRef]
15. Jing, F.; Gu, X.; Shen, X. Study on outgoing longwave radiation variations associated with strong earthquake. In Proceedings of the International Conference on Space Information Technology 2009, Beijing, China, 26–27 November 2009; SPIE: Bellingham, WA, USA, 2010; Volume 7651, pp. 275–280.
16. Yang, G.; Mi, Y. Thermal anomalies and earthquakes: Evidence from Wenchuan, China. *Earthq. Res. China* **2009**, *23*, 48–55.
17. Kong, X.; Li, N.; Lin, L.; Xiong, P.; Qi, J. Relationship of stress changes and anomalies in OLR data of the Wenchuan and Lushan earthquakes. *IEEE J. Sel. Top. Appl. Earth Obs. Remote Sens.* **2018**, *11*, 2966–2976. [CrossRef]
18. Zhang, W.; Zhao, J.; Wang, W.; Ren, H.; Chen, L.; Yan, G. A preliminary evaluation of surface latent heat flux as an earthquake precursor. *Nat. Hazards Earth Syst. Sci.* **2013**, *13*, 2639–2647. [CrossRef]
19. Cui, J.; Shen, X.; Zhang, J.; Ma, W.; Chu, W. Analysis of spatiotemporal variations in middle-tropospheric to upper-tropospheric methane during the Wenchuan M_s = 8.0 earthquake by three indices. *Nat. Hazards Earth Syst. Sci.* **2019**, *19*, 2841–2854. [CrossRef]
20. Akhoondzadeh, M. Ant Colony Optimization detects anomalous aerosol variations associated with the Chile earthquake of 27 February 2010. *Adv. Space Res.* **2015**, *55*, 1754–1763. [CrossRef]

21. Sekertekin, A.; Inyurt, S.; Yaprak, S. Pre-seismic ionospheric anomalies and spatio-temporal analyses of MODIS Land surface temperature and aerosols associated with 24 September 2013 Pakistan Earthquake. *J. Atmos.-Sol.-Terr. Phys.* **2020**, *200*, 105218. [CrossRef]
22. Shi, K.; Liu, X.; Guo, J.; Liu, L.; You, X.; Wang, F. Pre-earthquake and coseismic ionosphere disturbances of the M_w 6.6 Lushan earthquake on 20 April 2013 monitored by CMONOC. *Atmosphere* **2019**, *10*, 216. [CrossRef]
23. Ulukavak, M.; Yalçınkaya, M.; Kayıkçı, E.T.; Öztürk, S.; Kandemir, R.; Karslı, H. Analysis of ionospheric TEC anomalies for global earthquakes during 2000–2019 with respect to earthquake magnitude ($M_w \geq 6.0$). *J. Geodyn.* **2020**, *135*, 101721. [CrossRef]
24. Yang, M.; Zhang, X.; Ouyang, X.; Liu, J.; Qian, G.; Li, T.; Shen, X. Polarization Method-Based Research on Magnetic Field Data Associated with Earthquakes in Northeast Asia Recorded by the China Seismo-Electromagnetic Satellite. *Atmosphere* **2023**, *14*, 1555. [CrossRef]
25. Lin, J.T.; Melgar, D.; Thomas, A.M.; Searcy, J. Early warning for great earthquakes from characterization of crustal deformation patterns with deep learning. *J. Geophys. Res. Solid Earth* **2021**, *126*, e2021JB022703. [CrossRef]
26. He, M.; Wu, L.; Cui, J.; Wang, W.; Qi, Y.; Mao, W.; Miao, Z.; Chen, B.; Shen, X. Remote sensing anomalies of multiple geospheres before the Wenchuan earthquake and its spatiotemporal correlations. *J. Remote Sens.* **2020**, *24*, 681–700. [CrossRef]
27. Wei, C.; Zhang, Y.; Guo, X.; Hui, S.; Qin, M.; Zhang, Y. Thermal infrared anomalies of several strong earthquakes. *Sci. World J.* **2013**, *2013*, 208407. [CrossRef]
28. Jing, F.; Zhang, L.; Singh, R.P. Pronounced changes in thermal signals associated with the Madoi (China) M 7.3 earthquake from passive microwave and infrared satellite data. *Remote Sens.* **2022**, *14*, 2539. [CrossRef]
29. Jing, F.; Singh, R.P.; Cui, Y.; Sun, K. Microwave brightness temperature characteristics of three strong earthquakes in Sichuan Province, China. *IEEE J. Sel. Top. Appl. Earth Obs. Remote Sens.* **2020**, *13*, 513–522. [CrossRef]
30. Ye, Q.; Singh, R.P.; He, A.; Ji, S.; Liu, C. Characteristic behavior of water radon associated with Wenchuan and Lushan earthquakes along Longmenshan fault. *Radiat. Meas.* **2015**, *76*, 44–53. [CrossRef]
31. Qin, K.; Wu, L.; Zheng, S.; Ma, W. Discriminating satellite IR anomalies associated with the M_s 7.1 Yushu earthquake in China. *Adv. Space Res.* **2018**, *61*, 1324–1331. [CrossRef]
32. Zheng, S.; Wu, L.X.; Qin, K. Multiple parameters anomalies for verifying the geosystem spheres coupling effect: A case study of the 2010 M_s 7.1 Yushu earthquake in China. *Ann. Geophys.* **2014**, *57*, S0434.
33. Jing, F.; Shen, X.; Kang, C.; Xiong, P. Variations of multi-parameter observations in atmosphere related to earthquake. *Nat. Hazards Earth Syst. Sci.* **2013**, *13*, 27–33. [CrossRef]
34. Pulinets, S.; Ouzounov, D. Lithosphere–Atmosphere–Ionosphere Coupling (LAIC) model–An unified concept for earthquake precursors validation. *J. Asian Earth Sci.* **2011**, *41*, 371–382. [CrossRef]
35. Pulinets, S.; Ouzounov, D.; Karelin, A.; Davidenko, D. Physical bases of the generation of short-term earthquake precursors: A complex model of ionization-induced geophysical processes in the lithosphere-atmosphere-ionosphere-magnetosphere system. *Geomagn. Aeron.* **2015**, *55*, 521–538. [CrossRef]
36. Pulinets, S.; Budnikov, P.; Karelin, A.; Žalohar, J. Thermodynamic instability of the atmospheric boundary layer stimulated by tectonic and seismic activity. *J. Atmos.-Sol.-Terr. Phys.* **2023**, *246*, 106050. [CrossRef]
37. Pulinets, S.; Mironova, I.; Miklyaev, P.; Petrova, T.; Shitov, A.; Karagodin, A. Radon Variability as a Result of Interaction with the Environment. *Atmosphere* **2024**, *15*, 167. [CrossRef]
38. Gelaro, R.; McCarty, W.; Suárez, M.J.; Todling, R.; Molod, A.; Takacs, L.; Randles, C.A.; Darmenov, A.; Bosilovich, M.G.; Reichle, R.; et al. The modern-era retrospective analysis for research and applications, version 2 (MERRA-2). *J. Clim.* **2017**, *30*, 5419–5454. [CrossRef]
39. Piscini, A.; De Santis, A.; Marchetti, D.; Cianchini, G. A Multi-parametric climatological approach to study the 2016 Amatrice–Norcia (Central Italy) earthquake preparatory phase. *Pure Appl. Geophys.* **2017**, *174*, 3673–3688. [CrossRef]
40. Shen, X.; Zhang, X.; Hong, S.; Jing, F.; Zhao, S. Progress and development on multi-parameters remote sensing application in earthquake monitoring in China. *Earthq. Sci.* **2013**, *26*, 427–437. [CrossRef]
41. Hubbard, J.; Shaw, J.H. Uplift of the Longmen Shan and Tibetan plateau, and the 2008 Wenchuan (M = 7.9) earthquake. *Nature* **2009**, *458*, 194–197. [CrossRef]
42. Sun, J.; Yue, H.; Shen, Z.; Fang, L.; Zhan, Y.; Sun, X. The 2017 Jiuzhaigou earthquake: A complicated event occurred in a young fault system. *Geophys. Res. Lett.* **2018**, *45*, 2230–2240. [CrossRef]
43. Zhang, D.; Li, J.; Wu, Z.; Ren, L. Reconstructing the geometry of the Yushu Fault in the Tibetan Plateau using TLS, GPR and Trenching. *Remote Sens.* **2023**, *15*, 1994. [CrossRef]
44. Wei, G.; Chen, K.; Lyu, M.; Gong, W.; Dal Zilio, L.; Ye, L.; Tu, H. Complex strike-slip faulting during the 2021 M_w 7.4 Maduo earthquake. *Commun. Earth Environ.* **2023**, *4*, 319. [CrossRef]
45. Liu, X.; Chen, Q.; Yang, Y.; Xu, Q.; Zhao, J.; Xu, L.; Liu, R. The 2021 M_w 7.4 Maduo earthquake: Coseismic slip model, triggering effect of historical earthquakes and implications for adjacent fault rupture potential. *J. Geodyn.* **2022**, *151*, 101920. [CrossRef]

46. Liu, Q.; De Santis, A.; Piscini, A.; Cianchini, G.; Ventura, G.; Shen, X. Multi-parametric climatological analysis reveals the involvement of fluids in the preparation phase of the 2008 M_S 8.0 Wenchuan and 2013 M_S 7.0 Lushan earthquakes. *Remote Sens.* **2020**, *12*, 1663. [CrossRef]
47. Zhang, X.; De Santis, A.; Liu, J.; Campuzano, S.A.; Yang, N.; Cianchini, G.; Ouyang, X.; D'Arcangelo, S.; Yang, M.; De Caro, M.; et al. Pre-Earthquake Oscillating and Accelerating Patterns in the Lithosphere–Atmosphere–Ionosphere Coupling (LAIC) before the 2022 Luding (China) M_S 6.8 Earthquake. *Remote Sens.* **2024**, *16*, 2381. [CrossRef]
48. Cianchini, G.; Calcara, M.; De Santis, A.; Piscini, A.; D'Arcangelo, S.; Fidani, C.; Sabbagh, D.; Orlando, M.; Perrone, L.; Campuzano, S.A.; et al. The Preparation Phase of the 2023 Kahramanmaraş (Turkey) Major Earthquakes from a Multidisciplinary and Comparative Perspective. *Remote Sens.* **2024**, *16*, 2766. [CrossRef]
49. Schober, P.; Boer, C.; Schwarte, L.A. Correlation coefficients: Appropriate use and interpretation. *Anesth. Analg.* **2018**, *126*, 1763–1768. [CrossRef]
50. Liu, S.; Cui, L.; Wu, L.; Wang, Z. Analysis on the water vapor anomaly before Wenchuan earthquake based on MODIS data. In Proceedings of the 2009 IEEE International Geoscience and Remote Sensing Symposium, Cape Town, South Africa, 12–17 July 2009; IEEE: Cape Town, South Africa, 2009; Volume 2, pp. II-412–II-415.
51. Lu, X.; Meng, Q.; Gu, X.; Zhang, X.; Xiong, P.; Ma, W.; Xie, T. Study on multi-parameters of thermal infrared remote sensing anomalies of the Yushu earthquake. *Nat. Hazards Earth Syst. Sci. Discuss.* **2014**, *2*, 4439–4462.
52. Zhong, M.; Shan, X.; Zhang, X.; Qu, C.; Guo, X.; Jiao, Z. Thermal infrared and ionospheric anomalies of the 2017 M_w 6.5 Jiuzhaigou Earthquake. *Remote Sens.* **2020**, *12*, 2843. [CrossRef]
53. Ma, Y.; Liu, S.; Wu, L.; Xu, Z. Two-step method to extract seismic microwave radiation anomaly: Case study of M_s 8.0 Wenchuan earthquake. *Earthq. Sci.* **2011**, *24*, 577–582. [CrossRef]
54. Na, D.; Hongyue, L. Characteristics of Thermal Infrared Anomalies during the Earthquakes in Wenchuan, Lushan in Ya'an and Jiuzhaigou. In Proceedings of the IOP Conference Series: Earth and Environmental Science, Chongqing, China, 6–7 March 2021; IOP Publishing: Beijing, China, 2021; Volume 783, p. 012132.

Disclaimer/Publisher's Note: The statements, opinions and data contained in all publications are solely those of the individual author(s) and contributor(s) and not of MDPI and/or the editor(s). MDPI and/or the editor(s) disclaim responsibility for any injury to people or property resulting from any ideas, methods, instructions or products referred to in the content.